CrossMark

Photospheric and Chromospheric Magnetic Field Evolution during the X1.6 Flare in Active Region NOAA 12192

F. Ferrente[1], F. Zuccarello[1,2] , S. L. Guglielmino[2] , S. Criscuoli[3] , and P. Romano[2]

[1] Dipartimento di Fisica e Astronomia "Ettore Majorana"—Sezione Astrofisica, Università degli Studi di Catania, Via S. Sofia 78, I-95123 Catania, Italy; fabiana.ferrente@inaf.it
[2] INAF—Osservatorio Astrofisico di Catania, Via S. Sofia 78, I-95123 Catania, Italy; salvatore.guglielmino@inaf.it
[3] National Solar Observatory, 3665 Discovery Dr., Boulder, CO 80303, USA

Abstract

We report on observations acquired by the Interferometric Bidimensional Spectropolarimeter (IBIS) during SOL2014-10-22T14:02, an X1.6 flare that occurred in active region NOAA 12192, taken in the Fe I 617.30 nm and Ca II 854.2 nm line profiles. We analyze polarization signatures in the Stokes profiles of the two lines across one of the flare ribbons. Focusing our attention on the chromospheric signals and using the weak-field approximation (WFA), we study the temporal variation of the line-of-sight (LOS) magnetic field. We find variations of the magnetic field or the opacity along the flare ribbon, in most cases within the first 3 minutes of the observation just after the flare peak, during the tail of the flare impulsive phase. This result was validated by the STiC inversion of the pixels used for the WFA analysis. The analysis of the photospheric magnetic field shows that in this layer, the LOS magnetic field does not show the same changes observed in the chromosphere in the selected pixels, nor clear evidence of changes along the polarity inversion line around a magnetic polarity intrusion. In this respect, we also find that the temporal observing window is not suitable for assessing the presence of stepwise changes. The nonlinear force-free field extrapolations, together with the analysis of the ribbons' isophotes obtained from Interface Region Imaging Spectrograph data, suggest that the region corresponding to the magnetic intrusion observed by IBIS is characterized by a complex magnetic connectivity and is almost cospatial with the area affected by the initial energy release.

Unified Astronomy Thesaurus concepts: Active solar chromosphere (1980); Spectropolarimetry (1973); Solar flares (1496); High angular resolution (2167); Solar magnetic fields (1503)

1. Introduction

Measurements of the full vector magnetic field through Zeeman line-splitting observations are currently routinely carried out in the photosphere, based on spectropolarimetry. However, in order to get a more complete understanding of the magnetic field distribution in the solar atmosphere, such as when performing nonlinear force-free field extrapolations, it is very important to also retrieve the distribution of the chromospheric magnetic field (see, e.g., Vissers et al. 2021).

As reported by Harvey (2006), for many decades some researchers have carried out observations of the chromospheric magnetic field, for instance in sunspots and prominences. More recently, high-resolution spectropolarimetric observations in chromospheric lines have been carried out at several observatories: using the MultiRaies (MTR) mode at the Télescope Héliographique pour l'Étude du Magnétisme et des Instabilités Solaire (THEMIS; see, e.g., Ceppatelli & Briand 2001), the Advanced Stokes Polarimeter (ASP; Elmore et al. 1992), the Facility Infrared Spectropolarimeter (FIRS; Jaeggli et al. 2010), the Interferometric Bidimensional Spectrometer (IBIS; Cavallini 2006) at the Dunn Solar Telescope of the US National Solar Observatory (DST), the Crisp Imaging Spectro-polarimeter (CRISP; Scharmer et al. 2008) at the Swedish 1 m Solar Telescope (SST; Scharmer et al. 2003), and the GREGOR Infrared Spectrograph (GRIS; Collados et al. 2012) at the GREGOR telescope located at the Observatorio

del Teide in Tenerife. Nonetheless, these observations are currently still sparse and not routinely carried out. Indeed some difficulties can arise for two main reasons: (1) the number of diagnostics is limited to a few and (2) the photon count is typically low either because many chromospheric lines are in the UV and/or because of the low Landé factor (de la Cruz Rodríguez & van Noort 2017).

In this context, we also stress that, at the present time, only a few works deal with the measurements of magnetic fields in the chromosphere during flares, due to the paucity of slit-based or imaging spectropolarimetric data from the ground and the fortuitous possibility of observing flares.

In connection with flare studies, indeed many efforts to understand the chromospheric magnetic field via direct observations have been carried out, starting from the pioneering work of Penn & Kuhn (1995). Metcalf et al. (2005) used chromospheric magnetograms acquired by the Imaging Vector Magnetograph at the Mees Solar Observatory, which performs spectropolarimetric measurements across the Na I 589.6 nm line. They measured the total and the free magnetic energy in active region (AR) NOAA 10486 during the X10 flare that occurred on 2003 October 29.

Harvey (2012) analyzed spectropolarimetric data at $1''$ resolution acquired with the SOLIS vector magnetograph along the Ca II 854.2 nm line on 2011 November 8 during a C1.8 flare. Using Stokes I and V spectra and assuming the weak-field approximation (WFA), Harvey (2012) obtained an estimate of the line-of-sight (LOS) flux density in two flare kernels (415 G and -220 G). He also found an apparent strong variation of the chromospheric magnetic field B with height, as B appeared to increase toward higher layers.

Kleint (2012) investigated the decay phase of the C3.4 flare SOL2007-01-29T16:41, using full spectropolarimetric data taken with the IBIS at the DST. Measurements targeted the two footpoints of the flare. Using the chromospheric Ca II 854.2 nm line, she observed Stokes U profiles with asymmetric peaks, while Stokes V profiles indicated magnetic elements of the same polarity with large velocity shifts with respect to the photosphere, decreasing by a factor of two during the observing time.

Kuckein et al. (2015) reported on high-resolution observations acquired by the Tenerife Infrared Polarimeter (TIP; Martínez Pillet et al. 1999) instrument at the German Vacuum Tower Telescope in the near-infrared He I 1083 nm region, covering both the chromospheric He I triplet and the photospheric Si I line at 1082.7 nm during an M3.2 flare that occurred at 08:43 UT on 2013 May 17 in AR NOAA 11758. These observations covered all of the phases of the flare. Kuckein et al. (2015) found that He I Stokes V profiles were substantially larger than the usually larger photospheric Si I Stokes V profiles during the event. In the photosphere, the total magnetic field strength decreased during the flare and recovered its preflare configuration in about 30 minutes after the flare.

Judge et al. (2015) presented FIRS infrared data acquired at the DST from the X1-class flare SOL2014-03-29T17:48 and analyzed the Stokes profiles of Si I and He I 1083 nm lines. During the flare impulsive phase, in one of the flare ribbons, the He I line intensity reached twice the continuum intensity (I_c) and turned into emission. Linear polarization (LP) profiles characterized by the same sign were observed across the multiplet at $\lesssim 5\%$ of I_c. The analysis showed that weaker Zeeman-induced LP was also present, while hard X-ray (HXR) emission at 30–70 keV observed by the RHESSI satellite (Lin et al. 2002) was coincident only with the strongest LP. On the basis of non-LTE radiative transfer calculations, showing that the observed LP profiles could be justified by heating in slabs of optical depths $\lesssim 1$, the authors concluded that there is no requirement for colliding beams of particles, which on the other hand cannot give rise to the observed polarization.

Kleint (2017) detected stepwise variations in the chromospheric line-of-sight magnetic field (B_{LOS}) from spectropolarimetric observations along the Ca II 854.2 nm line taken with the IBIS at the DST during the same X1-class flare studied by Judge et al. (2015). Kleint (2017) also deduced B_{LOS} using the WFA, following Harvey (2012). This work reported a prevalence of decreased B_{LOS} (in absolute value) in the analyzed areas, as well as a different spatial distribution and intensity in the photosphere (i.e., near the polarity inversion line (PIL), with values ranging up to 320 Mx cm^{-2}) with respect to the chromosphere (i.e., close to loop footpoints, with larger values up to <640 Mx cm^{-2}). Furthermore, a spatial correlation between the changes in B_{LOS} and enhancements in coronal and chromospheric emission, as well as with HXR emission, was pointed out.

In the following years, other authors investigated the chromospheric magnetic field during flares. Libbrecht et al. (2019), from the analysis of He I D3 line emission during a C3.6 flare found evidence of condensations at the flare footpoints, where the magnetic field reached values of ~ 2500 G, together with weak upflows in the flare loop, where the magnetic field was weaker (0–500 G).

Vissers et al. (2021), studying an X2.2 flare, carried out inversions of the photospheric Fe I 630.2 nm line pair (Hinode SOT/SP data) using both Milne–Eddington and non-LTE atmospheric models, while data obtained in the chromospheric Ca II 854.2 nm line acquired by CRISP at the SST were analyzed using the WFA and non-LTE inversions. These results were compared with numerical models of the event. They found that the photospheric magnetic field strength was up to three orders of magnitude greater than that inferred from the numerical models. For the chromospheric magnetic field, Vissers et al. (2021) found a very good agreement between the results obtained with the spatially regularised WFA and those inferred from non-LTE inversions.

Yadav et al. (2021) analyzed a C2-class flare using data acquired by CHROMIS (Ca II K line) and by CRISP (Ca II 854.2 nm and Fe I 617.3 nm) at the SST. These authors found the presence of changes in the photospheric magnetic field during the flare, while, contrarily to previous studies on more energetic flares, the chromospheric magnetic field did not show any stepwise changes.

In this context, the aim of this work is to further investigate the properties of the changes in magnetic field occurring in active regions when flares take place: some of the works previously cited (e.g., Kleint 2017; Yadav et al. 2021) appear to have provided evidence of a different behavior of the chromospheric magnetic field during the respective analyzed flares. Some features, such as the changes in photosphere and chromosphere that are not spatially and temporally correlated, deserve to be further investigated to provide a more complete scenario of how the magnetic field responds to reconnection processes and to the successive phases of magnetic field rearrangement.

Here we present the analysis of Fe I 617.30 nm and Ca II 854.2 nm spectropolarimetric data acquired by the IBIS from a few minutes after the peak of the impulsive phase of an X1.6 flare that occurred in active region NOAA 12192 on 2014 October 22. Moreover, in order to place the characteristics of the active region in context, we also used magnetograms and images provided by the Solar Dynamics Observatory (SDO; Scherrer et al. 2012) satellite. Our analysis is carried out following a similar procedure used by Kleint (2017), but the data set that we used has two main differences. First, it does not cover all the flare evolution, referring to the phase immediately following the peak of the flare in soft X-rays, despite still encompassing the final part of the impulsive phase. Second, in Kleint (2017) the flare was associated with a filament eruption, while the data set analyzed in this work encompasses a magnetic field intrusion. The latter characteristic has a certain relevance because we can verify in a field of view containing both flare ribbons and the photospheric inversion line whether or not changes in the longitudinal magnetic field in the photosphere and chromosphere have a distribution similar to that found by Kleint (2017).

In the next section, we describe the observations and in Section 3 the data analysis. We present our findings in Section 4 and summarize our conclusions in Section 5.

2. Observations

The complex active region NOAA 12192 (hereafter, AR12192) appeared on 2014 October 17 on the solar disk; it was a recurrent AR and hosted the largest sunspot group in 25
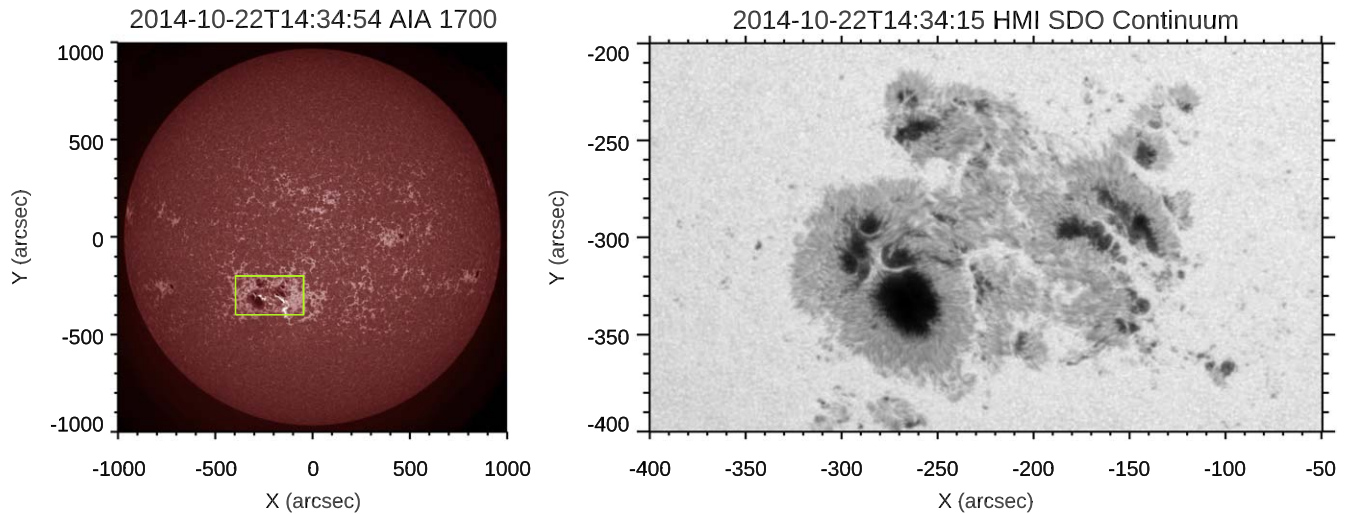
Figure 1. Left: context image of the solar atmosphere in an SDO/AIA 170 nm map, taken close in time to the peak of the X1.6 flare. The colored box indicates the FOV encompassing AR12192, used for the following analysis. Right: simultaneous SDO/HMI continuum image of AR12192. Here and in the following figures, north is at the top, west is to the right. The axes give the distance from the center of the solar disk.

years. On October 22, when it was located at S14E05, its area was about 2410 millionths of the solar disk (see Figure 1).

AR12192 was the most prolific flaring site of Cycle 24, being the source, from October 18 to 29, of 30 M- and 6 X-class flares. However, an unusual aspect of its flaring activity was the very poor correlation with eruptive events (see Thalmann et al. 2015; Ling & Kahler 2020). Previous studies of AR12192 showed that many of these flares were homologous, which could be an indication of a similar triggering mechanism taking place (e.g., Sui et al. 2004; Yang et al. 2014; Romano et al. 2015, 2018). Furthermore, Chen et al. (2015) showed that a strong confinement from the overlying magnetic field could be the reason for the poor production of coronal mass ejections (CMEs) in some active regions.

2.1. The X1.6 Flare

The X1.6 flare analyzed in this work sets a record in flare energy for an event without a CME. It occurred on 2014 October 22, started at 14:06 UT, peaked at 14:28 UT, and ended at 14:50 UT in GOES measurements (see Figure 2). SDO/AIA images reported in Figure 3 show the location of the flare ribbons in different atmospheric layers. In particular, we can notice that the eastern ribbon, included in the IBIS field of view (FOV) indicated with a green box, is located in the region hosting the largest following spot of the group, and is characterized in its northern part by the positive magnetic field intrusion (compare with Figure 3, top right panel).

In this work, the study of the following spot of AR12192 is performed using data with high temporal, spatial, and spectral resolution acquired by IBIS when it was operated at the NSO/DST. The observations were carried out on 2014 October 22 from 14:29 UT to 15:41 UT during good to excellent seeing conditions, aided by the high-order adaptive optics system (Rimmele 2004). The data set acquired on 2014 October 22 consists of 82 full spectropolarimetric scans through the Fe I 617.30 nm and Ca II 854.2 nm lines, and spectroscopic scans through the Hα 656.29 nm line with 51 s cadence. The observed FOV, which covers about $47\rlap{.}''5 \times 95''$ in the middle of the AR, is indicated in Figure 3 by a green box. The IBIS
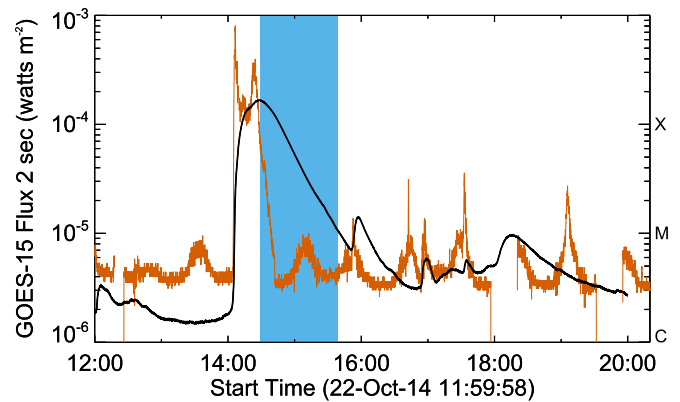

Figure 2. GOES X-ray flux reporting the time and the intensity of the X1.6 flare (solid black line), along with the HXR light curve deduced from RHESSI count rates in the 25–50 keV energy range (orange line). The IBIS instrument observed the eastern part of AR12192 immediately after the peak of the X1.6 flare. The shaded blue area indicates the time interval of IBIS observations.

pixel scale is $0\rlap{.}''095$ and the maximum spatial resolution is $\sim 0\rlap{.}''25$ (corresponding to ~ 180 km on the solar surface).

The time interval of acquisition for each spectral line is Ca II 854.2 nm (14:29:56–15:41:26 UT), Fe I 617.30 nm (14:29:32–15:41:00 UT), Hα 656.28 nm (14:29:52–15:41:20 UT). The lines were sampled with a spectral profile having an FWHM of 2 pm, an average wavelength step of 2 pm and an integration time of 80 ms. The Fe I 617.3 nm and Ca II 854.2 nm lines were sampled in spectropolarimetric mode with 20 and 25 spectral points, respectively. The Hα line was sampled in spectroscopic mode with 25 spectral points. However, the Hα data set is not used in this analysis.

The polarimetric sensitivity of IBIS measurements is about 0.01 in terms of the continuum intensity. After the standard calibration pipeline, residual crosstalk between Stokes I and Stokes Q, U, V is about 0.01 for the Ca II 854.2 nm line and 0.001 for the Fe I 617.3 nm line. Typical crosstalk values between Stokes V and Q/U are 0.1 for both lines.

For each spectral frame, a simultaneous broadband image was acquired at 636 nm. These images had the same FOV observed in spectropolarimetric or spectroscopic mode, with the same exposure time. To reduce the seeing degradation, the
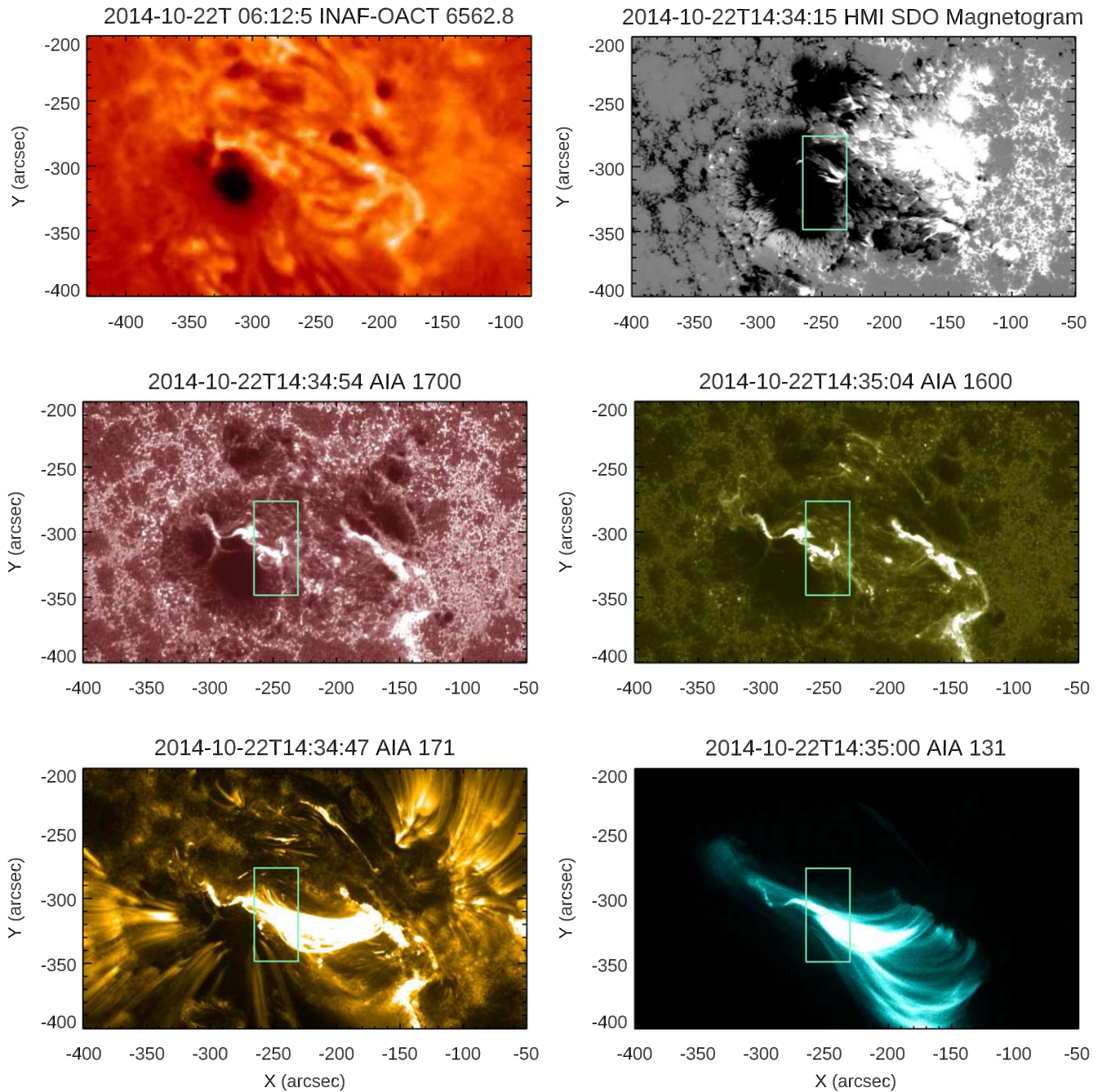
Figure 3. Top left: AR12192 observed by the Catania Solar Telescope a few hours before the beginning of the X1.6 flare in the Hα line core at 656.28 nm (Romano et al. 2022). Top right: SDO/HMI magnetogram of AR12192, simultaneous with the images shown in Figure 1. Note that the IBIS FOV, indicated with a green box, includes a region of negative polarity with some intrusions of positive polarity. Middle and bottom: cospatial SDO/AIA maps of AR12192, showing the flare ribbons a few minutes after the beginning of IBIS observations at different wavelengths.

narrowband data were destretched with respect to broadband images restored using the Kiepenheuer-Institut Speckle Interferometry Package (KISIP) code (Wöger et al. 2008).

We also analyzed continuum filtergrams and LOS magnetograms taken by the Helioseismic and Magnetic Imager (HMI; Scherrer et al. 2012) on board the SDO satellite (Pesnell et al. 2012) in the Fe I 617.3 nm with a resolution of 1″, as well as filtergrams acquired by the Atmospheric Imaging Assembly (AIA; Lemen et al. 2012).

On the same day, the Interface Region Imaging Spectrograph (IRIS; De Pontieu et al. 2014) satellite acquired a long-duration sequence, from 08:18 to 18:08 UT, which includes slit-jaw images (SJIs) in two passbands: C II at 133.0 nm and Mg II at 279.6 nm. We considered data acquired from 13:29 to 15:30 UT. The SJI filtergrams (224 for the interval of interest) have an FOV of 167″ × 174″, with an image rotation of 45° with respect to the north–south direction, and a temporal cadence of 33 s.

IBIS, SDO/HMI, and IRIS observations were coaligned using cross-correlation techniques, adopting as a reference the continuum filtergram closest in time to the flare peak taken by SDO/HMI at 14:34 UT on 2014 October 22. We used the IDL SolarSoft mapping routines to take into account the different pixel sizes.
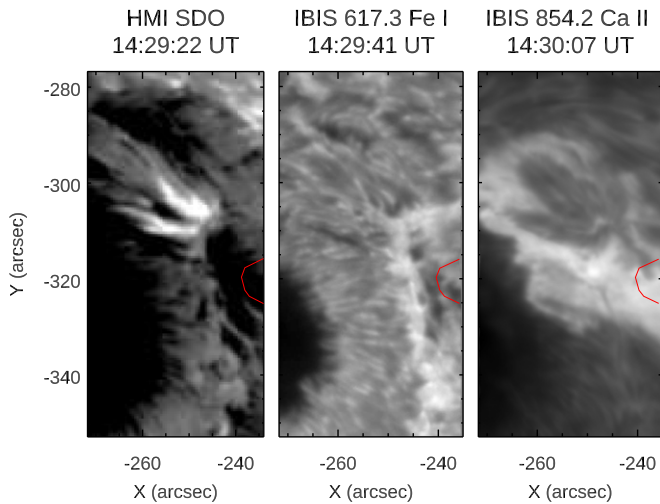
HMI SDO
14:29:22 UT

IBIS 617.3 Fe I
14:29:41 UT

IBIS 854.2 Ca II
14:30:07 UT

Figure 4. Left panel: a zoom of the SDO/HMI magnetogram acquired simultaneously with the start of IBIS observations, corresponding to the IBIS FOV. Middle panel: the first frame recorded by IBIS at the center of the Fe I line (showing the photosphere). Right panel: the first frame recorded by IBIS at the center of the Ca II line (showing the chromosphere). On each map we overplotted the RHESSI contours (red line), at 80% of the maximum intensity of the 25–50 keV energy range.

Finally, we also used RHESSI data acquired during the flare, in the interval 13:23—14:42 UT on 2014 October 22, focusing on the channel between 25 and 50 keV. We derived the light curve in this energy range and used the CLEAN algorithm (Hurford et al. 2002) to obtain the corresponding HXR image. For this purpose, we considered the front segment detectors (4F–5F–6F–7F–8F), using an integration time of 4 s after the intensity peak at 14:29:00 UT. Note that the potential pileup was not explicitly taken into account.

3. Data Analysis

3.1. IBIS Data Analysis

As already mentioned, IBIS observed the eastern flare ribbon of the X1.6 flare during the time interval from one minute after the flare peak, corresponding to the region characterized by the positive magnetic intrusion inside the negative polarity (see the green box in Figure 3, top right panel), in two different ranges of atmospheric height.

In Figure 4 we show sample images obtained in the photosphere and chromosphere by IBIS, as well as a comparison with the same FOV in the SDO/HMI magneto-gram closest in time to the beginning of IBIS observations.

3.1.1. Analysis of the Stokes Profiles

The analysis of spectropolarimetric data in the Fe I and Ca II lines during the flare evolution allows us to determine the variation in time of the Stokes profiles.

We selected three different locations, both in the photosphere and in the chromosphere, and we computed the average Stokes profiles (I, Q, U, and V) in a box 10×10 pixels wide (see Figure 5). The three boxes are indicated with small squares of three different colors (green, blue, and red), corresponding to the color scheme used for the plots in Figure 5. As we can note from Figure 5 (bottom), in the chromosphere the three boxes are all located on the ribbon, but they correspond to different photospheric configurations. In the photosphere the red box is located on a pore to the west of the following sunspot, the

green box is located on a penumbral filament, and the blue box on a bright photospheric area at the border of the penumbra.

We calculated the mean value of intensity in the continuum in a quiet-Sun region within the FOV, $\langle I_c \rangle$, and we normalized the Stokes parameters to this value.

In Figure 5 we show, in the top panel, the Stokes profiles analyzed in the photosphere and, in the bottom panel, the Stokes profiles for the same locations in the chromosphere, where they are along the ribbon.

We can see that Q and U are stronger in the chromosphere than in the photosphere (where the Q and U signals in some pixels are even below the IBIS sensitivity level) and that they seem to have profiles unrelated to each other, indicating that linear polarization at the location corresponding to the boxes in Figure 5 may have no correlation in the two layers. The profiles of Q and U in the photosphere show different shapes in the three boxes.

3.1.2. Circular and Linear Polarization in the Chromosphere

Spectropolarimetric data also provide information on the presence of linear and circular polarization in the flaring site.

From Stokes parameters I, Q, U, and V it is possible to compute circular polarization (CP) and linear polarization (LP) signals (e.g., del Toro Iniesta 2007). In particular,

$$ \text{LP} = \frac{1}{n \langle I_{\text{cont}} \rangle} \sum_{i=n_i}^{n_f} \sqrt{Q_i^2 + U_i^2} \tag{1} $$

and

$$ \text{CP} = \frac{1}{n \langle I_{\text{cont}} \rangle} \sum_{i=n_i}^{n_f} \epsilon_i V_i \tag{2} $$

with

$$ \epsilon_i = \begin{cases} 1 & i < m \\ 0 & i = m \\ -1 & i > m \end{cases} \tag{3} $$

where n is the number of spectral points considered and $\langle I_{\text{cont}} \rangle$ is the intensity mean value in the continuum calculated as described in Section 3.1.1. We choose only the central part of the line, by selecting 19 spectral points for the Ca II 854.2 nm line. n_i and n_f are the initial and the final indices, and m is the index of the spectral point located at the center of the line.

We computed the linear and the circular polarization for all the pixels in each frame. To properly reconstruct the sign of CP in the Ca II line, we reversed the sign of Stokes V in the pixels where we found Stokes I in emission.

In Figure 6 we can see the results obtained through the measurement of linear and circular polarization pixelwise in the flare image at two different times in the chromosphere.

Using a color code specified in the color bar and within a specific range of values in order to increase the contrast of the images for a better visualization, we plotted the LP and CP of the regions where $\sqrt{Q_i^2 + U_i^2}$ was greater than $3\sqrt{\sigma_Q^2 + \sigma_U^2}$ for the linear polarization, and where Stokes $|V|$ was three times greater than σ_V, with σ_Q, σ_U, and σ_V being the standard deviations of the three Stokes parameters, respectively. All these signals are above $0.01I_c$, i.e., above the polarimetric sensitivity of the IBIS instrument. As we can see by comparison of the two panels relevant to the chromosphere (see Figure 6), both LP and negative CP are located mainly along the flare ribbon. Moreover, their intensity decreases over time.
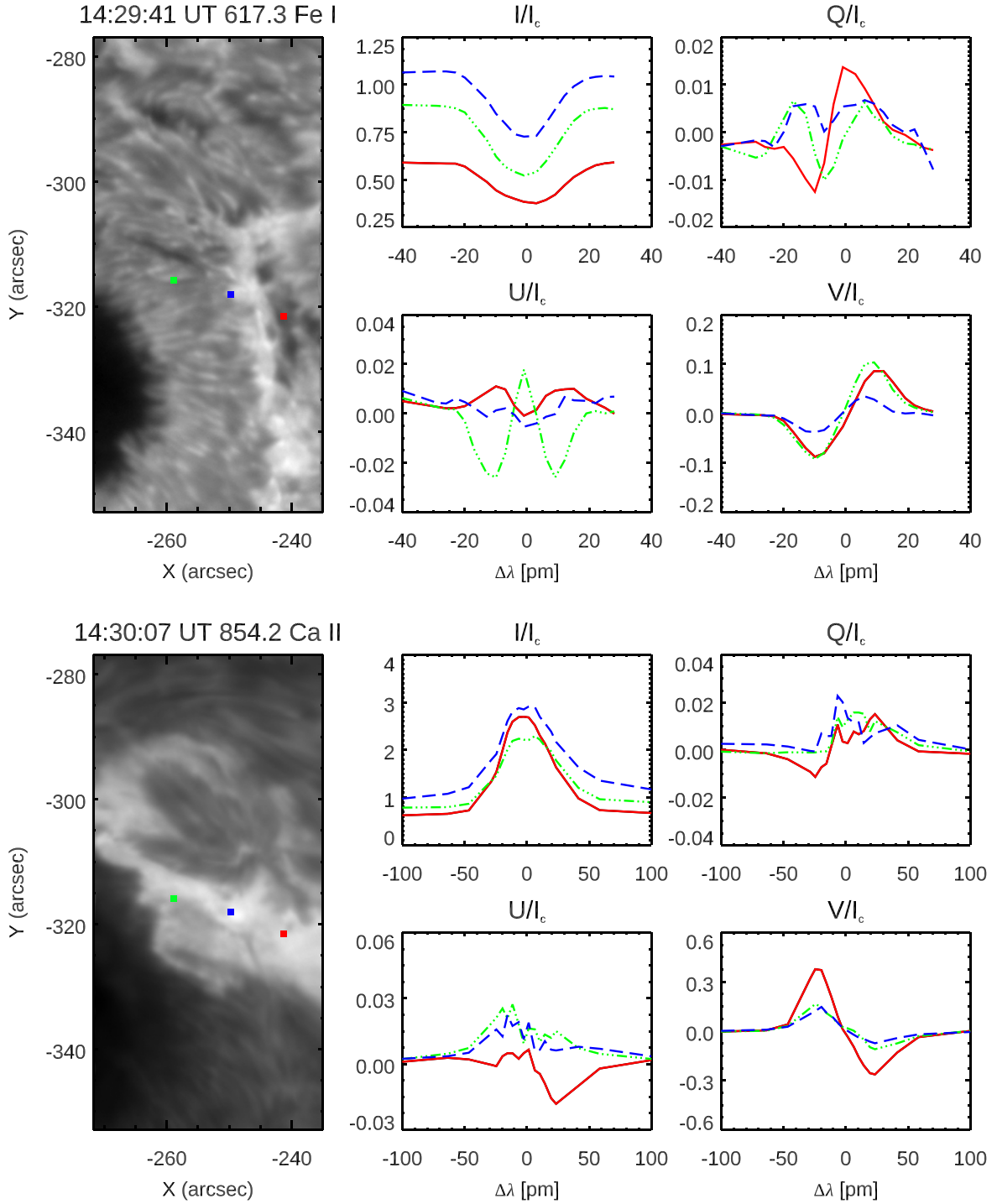
Figure 5. Top: the left panel shows the three boxes selected in the photosphere. The plots on the right show the corresponding Stokes profiles. Bottom: the left panel shows the three boxes selected in the chromosphere. The plots on the right show the corresponding Stokes profiles.

This is likely related to the enhanced emission observed during the flare: the polarization increases most in parts where the emission is higher, and decreases with decreasing emission during the gradual phase of the flare.

3.2. Determination of the Magnetic Field

3.2.1. Weak-field Approximation

We computed the flux density of the longitudinal magnetic field with the weak-field approximation (Landi Degl'Innocenti 2008). Indeed, to first order in B, there is a relationship between Stokes V

and $dI/d\lambda$, from which it is possible to obtain the value of the magnetic field along the line of sight.

We used a least-squares minimization of the form proposed by Martínez González & Bellot Rubio (2009), as follows:

$$\frac{\partial}{\partial \Phi}\left[\sum_i\left(V_i + \Phi C \frac{\partial I}{\partial \lambda_i}\right)^2\right] = 0 \qquad (4)$$

where we indicate with the subscript i the different values of the parameters across the entire profile of the line.
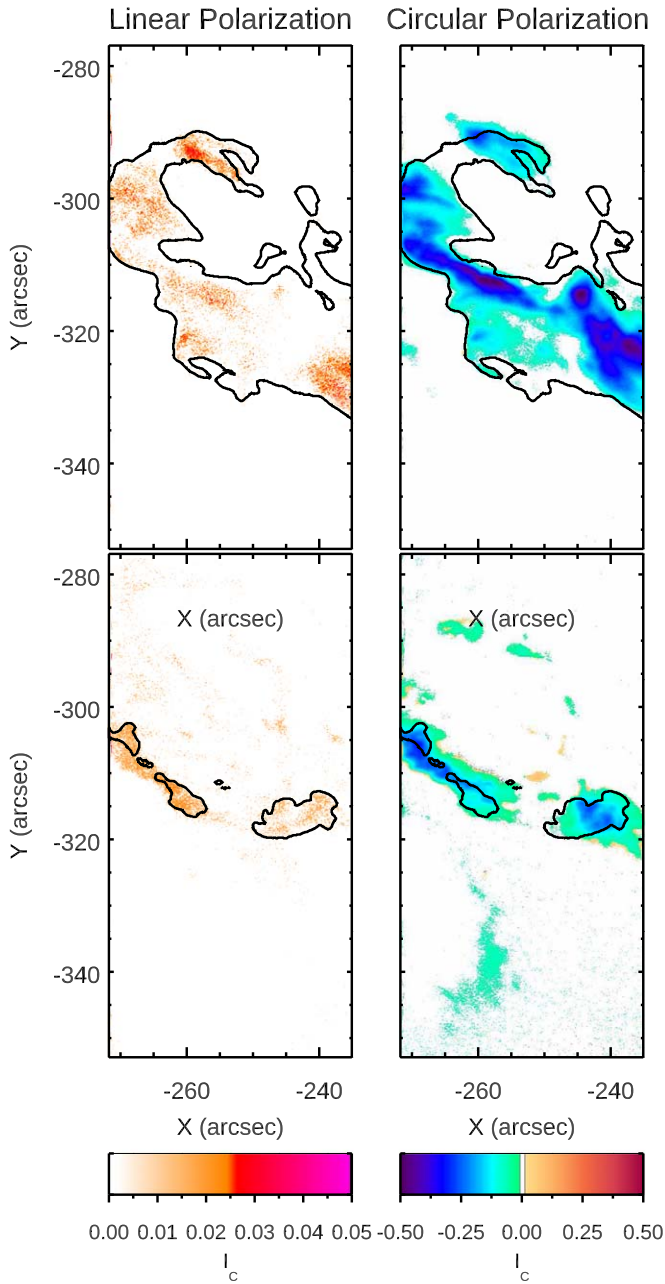
Figure 6. Maps of the polarization signals in the chromosphere. The left panels show maps of the linear polarization and the right panels maps of the circular polarization, at two observing times (14:30 UT, top; 15:31 UT bottom). The black contour highlights the position of the ribbon.

Therefore, the value of the magnetic flux density Φ, corresponding to B_{LOS}, can be obtained from

$$\Phi = -\frac{\sum_i \left(\frac{\partial I}{\partial \lambda_i} V_i\right)}{C\sum_i \left(\frac{\partial I}{\partial \lambda_i}\right)^2} \quad (5)$$

where the constant C is equal to $4.6686 \times 10^{-13}\lambda_0^2 \bar{g}$, with $\bar{g}$ the Landé factor and λ_0 the central wavelength of the selected spectral line expressed in angstrom.

We carried out similar analysis steps as Kleint (2017) to derive information about the magnetic configuration of the
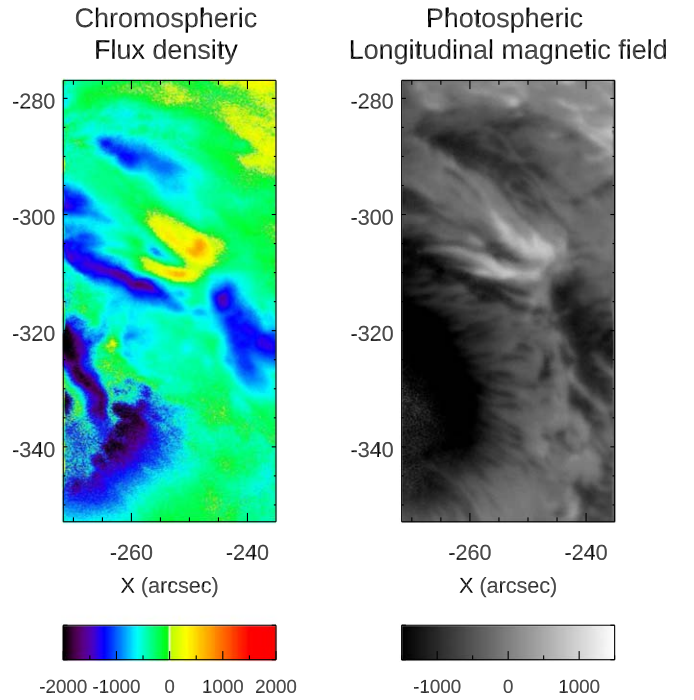

Figure 7. Left: map of the LOS magnetic flux density in the chromosphere obtained using the WFA (Equation (5)) at 14:30:07 UT. Right: map of photospheric B_{LOS} obtained for the first frame with P-MILOS.

flaring chromosphere based on the Ca II data, using the Landé factor $\bar{g} = 1.1$ for the Ca II 854.2 nm line.

We performed the calculation for each pixel in the FOV, obtaining the result shown in the left panel of Figure 7. This displays the result of the WFA calculation, for a selected best-seeing frame at the beginning of the IBIS observations, 14:29 UT, and shows the B_{LOS} map in the chromosphere. We can see that the region of positive intrusion, exhibiting a longitudinal magnetic field strength of the order of $B \sim 200$ G, is surrounded by a large negative region with $B \sim -100$ G.

3.2.2. Spectropolarimetric Inversions of Ca II

After determining the longitudinal magnetic field with the WFA, we decided to validate the results with spectropolarimetric inversions, inverting some selected pixels of the IBIS Ca II data (see Section 3.3) with the STiC code (de la Cruz Rodríguez et al. 2019).

The IBIS wavelength grid was not equispaced so we used a finer equispaced grid that contains all the observed spectral points as a subset. Then we gave nonzero weights only to the observed spectral points and zero weights to the fictitious spectral points.

We represented the IBIS instrumental profile of the Ca II 854.2 nm line with a Gaussian of 4.3 pm (Reardon & Cavallini 2008), as STiC convolves the instrumental profile inserted with the synthetic profiles during the inversion. We started the first cycle of inversion with a model atmosphere derived from the FAL-C model (Fontenla et al. 1993), and interpolated 63 depth points from $\log \tau_{500} = -7.8$ to $\log \tau_{500} = 1$, where τ_{500} is the optical depth of the continuum at 500 nm.

For each pixel to invert, we used three different cycles as proposed by Yadav et al. (2021; see Table 1), using for the

Table 1
Number of Nodes Used to Run the STiC Code for the Temperature T, LOS Velocity (V_{LOS}), Turbulent Velocity (V_{turb}), LOS Magnetic Field (B_{LOS}), Horizontal Magnetic Field ($B_\perp$), and Azimuth (Φ) during Each Cycle of the Inversion

Parameters	Cycle 1	Cycle 2	Cycle 3
T	7	9	10
V_{LOS}	2	5	7
V_{turb}	1	3	5
B_{LOS}	1	2	3
$B_\perp$	1	2	3
Φ	1	1	2

second and third cycles the new model atmosphere retrieved from the previous cycle.

3.2.3. Milne–Eddington Inversion of Fe I Data

For the analysis of the Fe I line, we used the P-MILOS code, which is an open-source Milne–Eddington Stokes inversion code written in C (Bellot Rubio et al. 2022).

We adopted a Milne–Eddington model atmosphere as an initial guess for the model. We retrieved from Reardon & Cavallini (2008) the value of the instrumental profile of IBIS (2.25 pm) at 617.3 nm, which has to be inserted in P-MILOS to be convolved with the synthetic spectra. Due to the fact that the wavelength grid has to be equispaced, we neglected the first value of the grid. For each frame, we obtained magnetograms similar to that shown in the right panel of Figure 7.

3.3. Determination of the Changes in Magnetic Field

From previous studies (e.g., Sudol & Harvey 2005; Kleint 2017), it is known that the temporal variation of the magnetic field occurring during a flare in certain locations can be characterized to first order by a step function.

Sudol & Harvey (2005) showed that abrupt, significant, and permanent changes of the photospheric magnetic field are common features of X-class flares (see the reviews of Wang & Liu 2015; Toriumi & Wang 2019; and references therein). This has been shown also in statistical studies (Castellanos Durán et al. 2018; Castellanos Durán & Kleint 2020).

Using the same methods, Kleint (2017) found that chromospheric magnetic changes during an X1-class flare were stronger and more extended than the photospheric changes. In addition, it was also found that chromospheric changes predominantly occur near the footpoints of coronal loops.

In order to determine whether B_{LOS} exhibits a relevant change in some locations during the event that we studied, we fitted the evolution of B_{LOS} during the IBIS sequence with the same step function as Sudol & Harvey (2005):

$$B(t) = a + bt + c\left\{1 + \frac{2}{\pi}\arctan[n(t - t_0)]\right\} \quad (6)$$

where a, b, c, n, and t_0 are the free parameters of the fit. a and b take into account the strength and the evolution of the background field, t is the time, c is the half-amplitude of the step, π/n is the time interval in which the change occurs, dt, and t_0 is the midpoint of the step. $2c$ is the amplitude of the step and it represents a measure of the change in the magnetic field, dB.

We used the Levenberg–Marquardt method of nonlinear least-squares minimization to compute the fit between the magnetic field, B_{LOS} calculated with the WFA, and the time, using the MPFITFUN routine in IDL. We applied this method only to the regions in the FOV where the signal of Stokes V was greater than $3\sigma_V$ for the entire duration of the data set.

In addition, we performed a geometrical correction to measure the size of the step using a method proposed by Castellanos Durán et al. (2018). With this method we can also take into account the effective duration of the step (π/n) and the slope of the background b. According to Castellanos Durán et al. (2018), we calculated two straight lines intercepting the stepwise function at the start and at the end of the step, respectively, parallel to the background field.

$$B(t_e) = bt_e + c \quad (7)$$

and

$$B(t_s) = bt_s + c \quad (8)$$

where $t_s = t_0 - \pi/2n$ is the time at the start of the step and $t_e = t_0 + \pi/2n$ is the time at the end of the step. Similarly to Castellanos Durán et al. (2018), the distance between the two parallel straight lines is the size of the change, which is given by $\Delta B_{LOS} = \Delta B_{LOS}(t_e) - \Delta B_{LOS}(t_s) - \pi b/n$ (note a factor of 2 different from Castellanos Durán et al. 2018).

We compared the results obtained with the two methods and we selected the smaller of the two as the amplitude of the change in magnetic field.

We computed the fit for all the pixels in the frames. We set all the parameters of the fit to zero if the magnetic field variation was too large, $|dB| = |2c| > 600$ G, or too small, -50 G $< dB < 50$ G, and if the magnetic field jump occurred during too long a period, $dt = \pi/n > 5$ minutes. We also performed a manual verification of the fits obtained, setting B_{LOS} equal to zero where we noted a failure of the fit.

Using the Ca II line, we obtained the maps presented in Figures 8(a) and (b). On the left panel, we show on a color scale the location of the changes in magnetic field in the chromosphere during the time interval analyzed, about 15 minutes. On the right panel, we show the duration of the change, dt, for the selected pixels. We notice that changes occur in small, coherent areas located at the core of the ribbon.

Comparing the two maps shown in the first two panels of Figure 8, we find that, on average, a longer duration of the change in magnetic field is observed in the ribbon regions where the variation of B_{LOS} is stronger.

In Figure 8(d) we display some examples of the evolution in chromospheric magnetic field in pixels showing changes obtained by means of the WFA analysis, whose location is shown in Figure 8(c). The figure also shows a comparison between the evolution of the longitudinal magnetic field in the chromosphere (colored circles) and the mean intensity (inverted triangles) at four different locations in the FOV. The temporal evolution of the mean intensity and that of the longitudinal magnetic field seem to show different trends. We can see an increase in intensity at the beginning of the data set, which corresponds also to an apparent increase in the magnetic field, but we can notice that afterwards the intensity shows a decrease, while the changes in the longitudinal magnetic field appear to be persistent.

It is worth noticing that all changes occur in the very first phases of the flare evolution, just after the peak of the flare. The
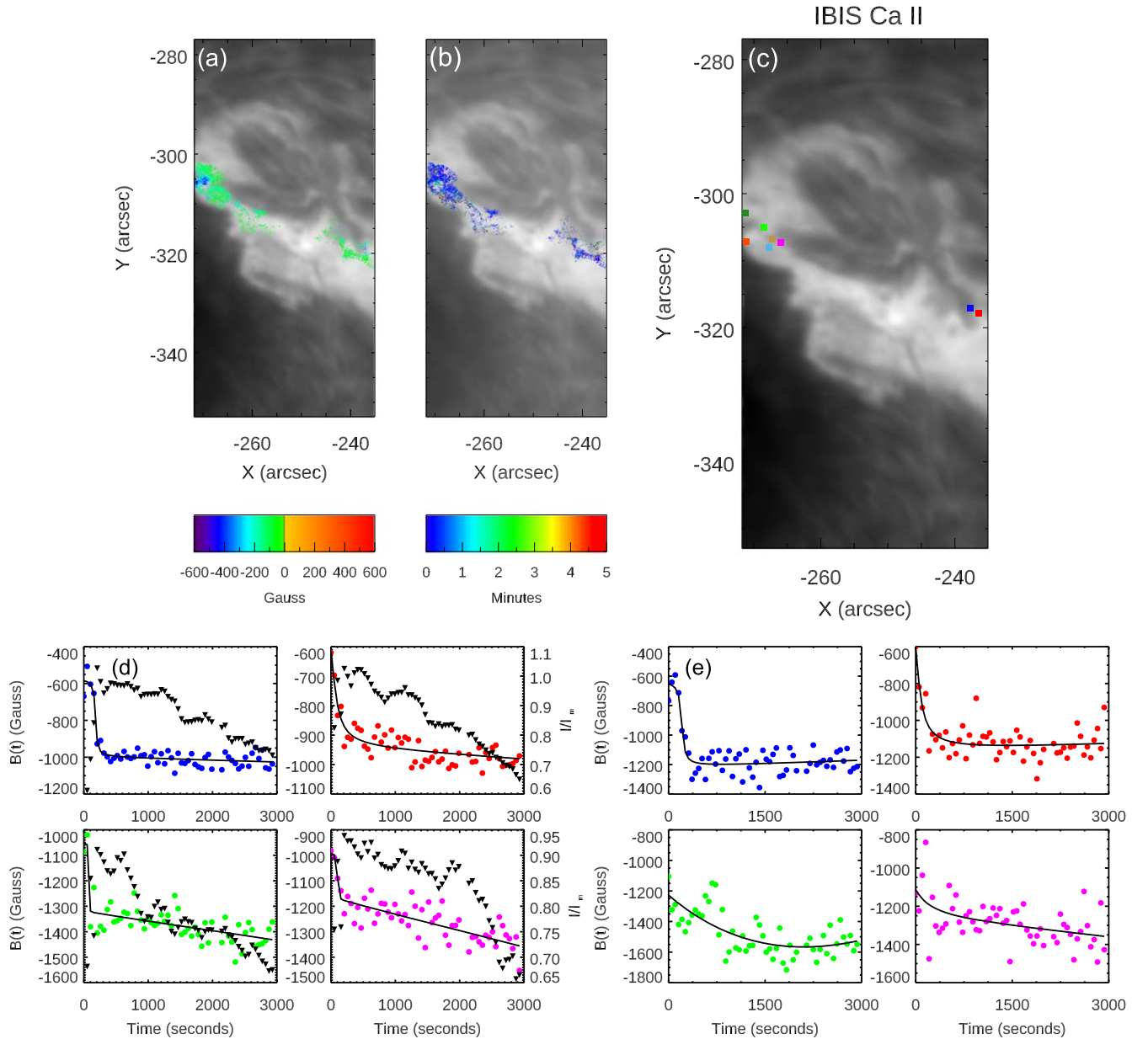
Figure 8. (a) Locations of the points with variation of B_{LOS} in the chromosphere (see the main text). The color scale indicates the magnitude of the variation. (b) Map of dt (minutes) on a color scale. (c) Locations of the boxes used to obtain the B_{LOS} evolution shown in the bottom panels and in Figure 9. (d) Temporal evolution of the changes in chromospheric B_{LOS} obtained using the WFA in four different pixels indicated by the colored boxes in the top right panel. The inverted black triangles show the evolution of the mean intensity. (e) Temporal evolution of the chromospheric B_{LOS} obtained with STiC in the same four pixels indicated by colored boxes in the top right panel.

analysis of the count rates deduced from RHESSI data indicates that the hard X-ray emission in the nonthermal energy range of 25–50 keV dropped from its maximum at 14:24 UT (about 1.8×10^3 corrected DN s^{-1}) by a factor of 10 at 14:34 UT (see Figure 2).

This suggests that during the first minutes of the IBIS observations the flare was still in the tail of its impulsive phase.

We compare the magnetic field values obtained with the WFA over time with those retrieved by the STiC inversions, as shown in Figure 8(e). We note that, in the analyzed pixels, the evolution of the longitudinal magnetic field shows trends of the same order of magnitude as those obtained using the WFA.

Figure 9(a) displays the temporal evolution of four additional pixels, obtained with the WFA, alongside the corresponding comparison obtained through STiC (panel (b)). Their location

is shown in Figure 8(c). The dark green and orange circles in the second column serve as examples of the fits that were discarded during the manual inspection of the results of the fitting algorithm.

For the analyzed pixels we verified that there is no strong correlation between the longitudinal magnetic field and the emission (Figure 10). With regard to this point, we computed the correlation over time between $dI/d\lambda$ and B_{LOS}, as well as Stokes I and B_{LOS} for all the pixels with a change in the FOV. We evaluated the square of the Bravais–Pearson parameter r^2 for these pixels and we found that it ranges between 0.1 and 0.3. This indicates a low correlation between these quantities.

We also fitted the B_{LOS} values retrieved by P-MILOS for the Fe I data with the same step function (Equation (6)) as used for the chromospheric B_{LOS} deduced from Ca II data, to investigate
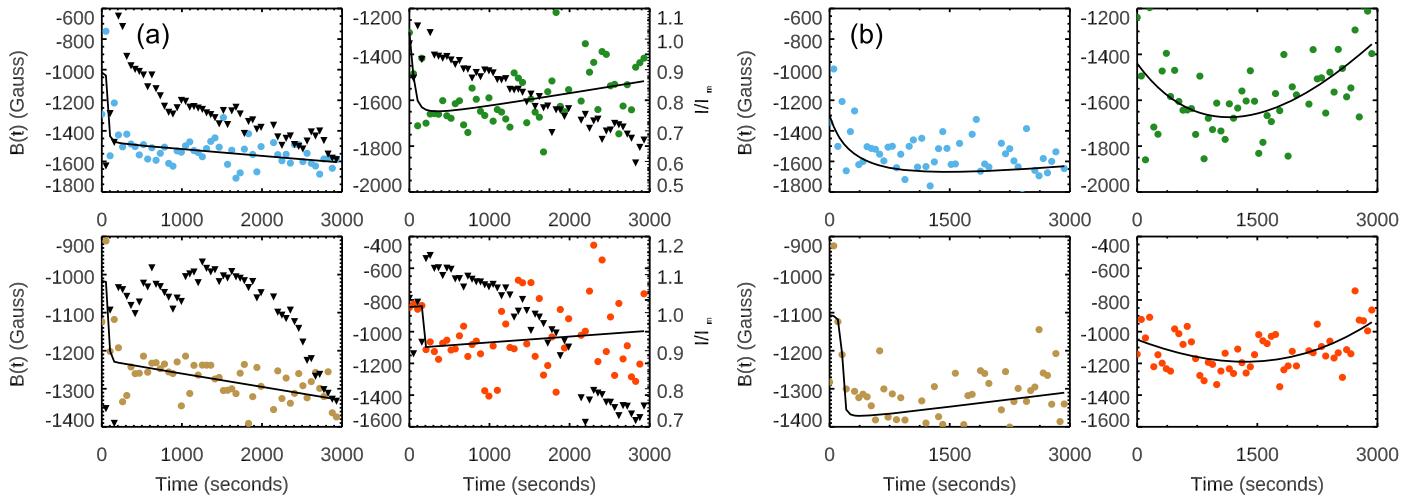
Figure 9. (a) Temporal evolution of the changes in chromospheric B_{LOS} obtained using the WFA, as in Figure 8(d), for four additional pixels. The inverted black triangles show the evolution of the mean intensity. The cyan and the light brown circles represent two additional examples of what we identified as permanent changes, while the dark green and the orange circles are two examples of fits rejected by our manual examination of the outcomes of the fitting routine. (b) Temporal evolution of the chromospheric B_{LOS} obtained with STiC in the same four pixels shown in (a).

whether there are changes also in the photosphere. Using the method described previously, we obtained the maps shown in Figures 11(a) and (b). It is possible to notice that in our analysis of the photospheric IBIS data set, beginning shortly after the flare peak, we could not identify the same coherent patches as identified by Castellanos Durán et al. (2018; see their Figure 2 FL11). Taking into account that these authors utilized a time interval of 90 minutes centered on the flare maximum for their analysis, we evaluated the stepwise photospheric changes over a comparable time period using HMI data in the IBIS field of view. As we can see in Figure 11(d), we obtained a small coherent patch at the edge of the IBIS FOV, which is consistent with the result obtained by Castellanos Durán et al. (2018). These changes do not take place along the PIL but at least 10″ away from it.

We also evaluated the longitudinal stepwise changes with HMI over a period of time comparable to that of the IBIS data set (Figure 11(c)), demonstrating that if we take into account a time interval starting just after the flare peak, we are also unable to observe the same photospheric changes with HMI. This indicates that, even if our analysis may suggest the presence of stepwise chromospheric changes at certain locations, the restricted observing time interval prevents us from being certain that the observed changes are permanent on a more global timescale. Moreover, many changes may be missed when observing only the second part of the flare, after the peak.

Figure 12(a) reports the evolution of the photospheric longitudinal magnetic field in the same pixels analyzed in Figure 8.

In order to validate the results obtained from the analysis of the photospheric IBIS observations, we compared them with SDO/HMI data. Due to the different resolutions of the two data sets, we evaluated for the IBIS photospheric data the values of the LOS magnetic field in 11×11 boxes in the FOV, corresponding to 3×3 boxes in the HMI FOV (Figures 12(b) and (c)). To analyze the temporal variation of the longitudinal magnetic field we choose the data series taken every 45 s. We created submaps with the same FOV as IBIS, and we aligned all the 120 frames taking into account the solar rotation with the SolarSoft routine `rot_xy`.
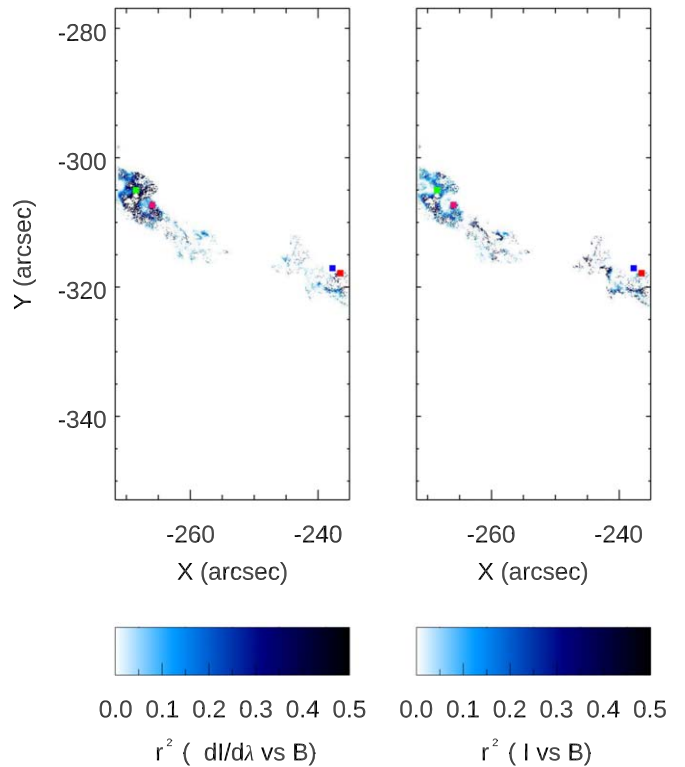

Figure 10. Correlation maps between B_{LOS} and quantities linked to the Stokes I emission. Pixels indicated with colored boxes are the same as those analyzed in Figure 8.

After aligning all the selected 120 frames, we plotted in Figure 12(b) the temporal evolution of the same boxes shown in Figure 12(a). We can note from the comparison between the two sets of graphs that the values of B_{LOS} we obtained with the P-MILOS inversion of IBIS data are consistent with those deduced from SDO/HMI data, except for the green box, which shows higher values in the IBIS data. It is important to stress in this context that the comparison with SDO/HMI data might not be fully reliable because the alignment process in SDO/HMI data is quite critical, due to the lower resolution of the filtergrams. Also, the oscillating trend that characterizes the
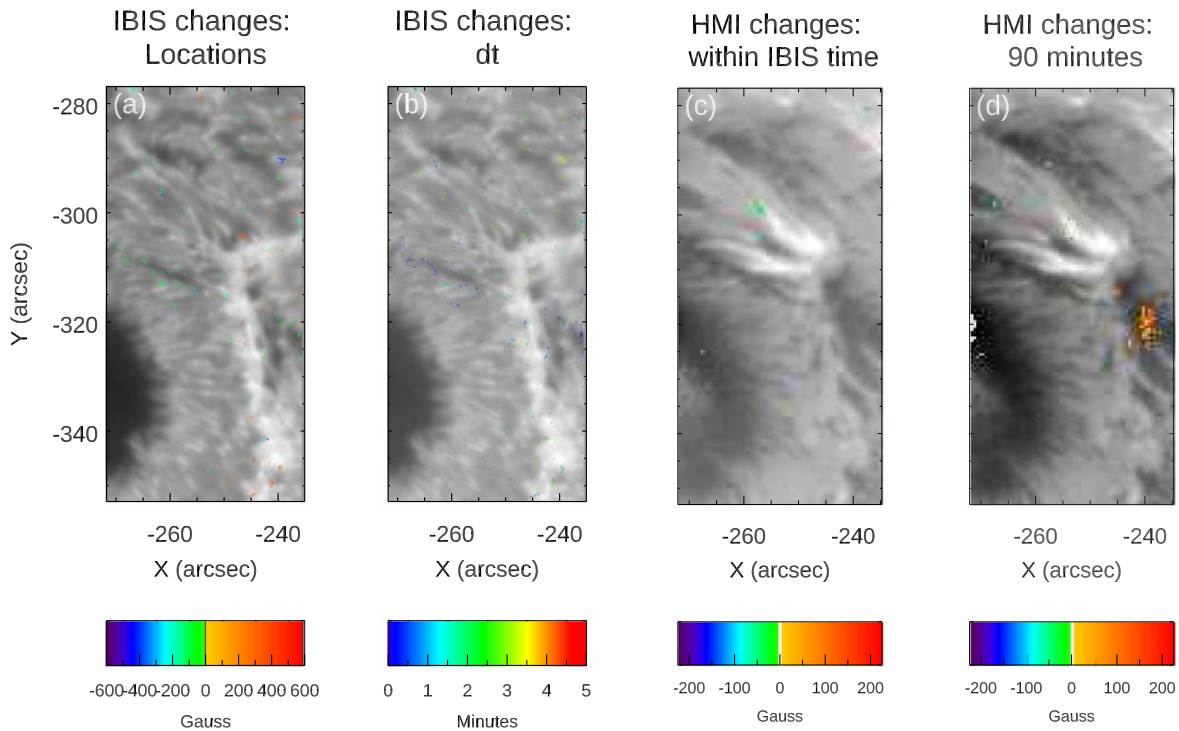
Figure 11. (a) Locations of the points with variations of B_{LOS} in the photosphere superposed on a photospheric image acquired in the core of the Fe I 617.3 nm line. The color scale indicates the magnitude of the variation. (b) Map of *dt* (minutes) on a color scale. (c) Locations of the points with variations of B_{LOS} in the photosphere obtained with HMI in the same temporal interval as the IBIS data set. (d) Locations of the points with variations of B_{LOS} in the photosphere obtained with HMI in a time interval of about 90 minutes centered at the peak of the flare.

longitudinal magnetic field recorded by SDO/HMI is due to aligning issues.

3.4. Magnetic Field Extrapolation Using SDO/HMI Magnetograms

The spatial resolution of the available AIA images of the corona is not sufficient to investigate in detail the connectivity of the regions of the ribbon where the temporal variation of the LOS magnetic field has been observed. For this reason, we performed the nonlinear force-free field (NLFF) extrapolation using a method proposed by He et al. (2011). This method is based on the formulation of the direct boundary integral equation (Yan & Li 2006). For our goal we used as boundary conditions the Space-weather Active Region Patches (SHARPs) version (Hoeksema et al. 2014) of the vector magnetograms taken by SDO/HMI on October 22 at 14:00 UT, i.e., some minutes before the flare onset. We used as input for the extrapolation a rebinned version of the magnetograms to reduce the computational time: we used 266×166 pixel arrays corresponding to an FOV of $400'' \times 250''$, i.e., changing the pixel scale from $0\rlap{.}''5$ to $2\rlap{.}''0$.

The output 3D coronal magnetic field was $266 \times 166 \times 148$ grids with the photospheric magnetogram being retained in the output 3D data as the bottom layer (layer 0) of the data cube (see Romano et al. 2019 for further details).

The left and right panels of Figure 13 show the side and top views of the NLFF extrapolation, respectively. The blue and green flux tubes indicate the connectivity of the positive structures observed by IBIS near the main negative spot of the AR (clearly visible in the first panel of Figure 4). These two magnetic flux systems are overarched by the gray field lines connecting the negative patch in between the above-mentioned

positive structures with a positive-polarity area located in the south of the preceding sunspot.

In particular, we identify two lower systems of field lines (indicated by blue and green lines in Figure 13) that connect the ribbon observed by IBIS with the positive structures highlighted in the first panel of Figure 4, while a higher system of field lines (yellow lines in Figure 13) seems to connect the same ribbon with the ribbon located outside the IBIS FOV, corresponding to the positive sunspots on the western side of the AR.

As shown in the bottom panels of Figure 13, by means of the comparison between the extrapolation and the IRIS image taken at the beginning of the flare, we can see that the ribbon located inside the IBIS FOV and the subject of the present study may be ascribed to the acceleration of particles along field lines corresponding to different magnetic systems. Indeed, the maximum of the HXR emission detected by the RHESSI satellite at around 14:24 UT seems to match exactly with the location of the area where both the yellow and green field lines are close to each other.

The coherence of our extrapolations with those reported in previous works, in particular those obtained by Kleint et al. (2018), is noteworthy.

We also analyzed the temporal evolution of the ribbon isophotes in the IRIS FOV, considering the onset of the flare as a reference image (14:06 UT), for both C II and Mg II. Then, on the reference images we plotted the isophotes with a cadence of ∼8.5 minutes during the subsequent flare evolution (see Figure 14). The corresponding time of the isophotes is specified with a color scheme.

We can see from Figure 14 that the motion of the ribbons is very slow and the displacement is small, confirming what has been observed by other authors about the ribbon separation
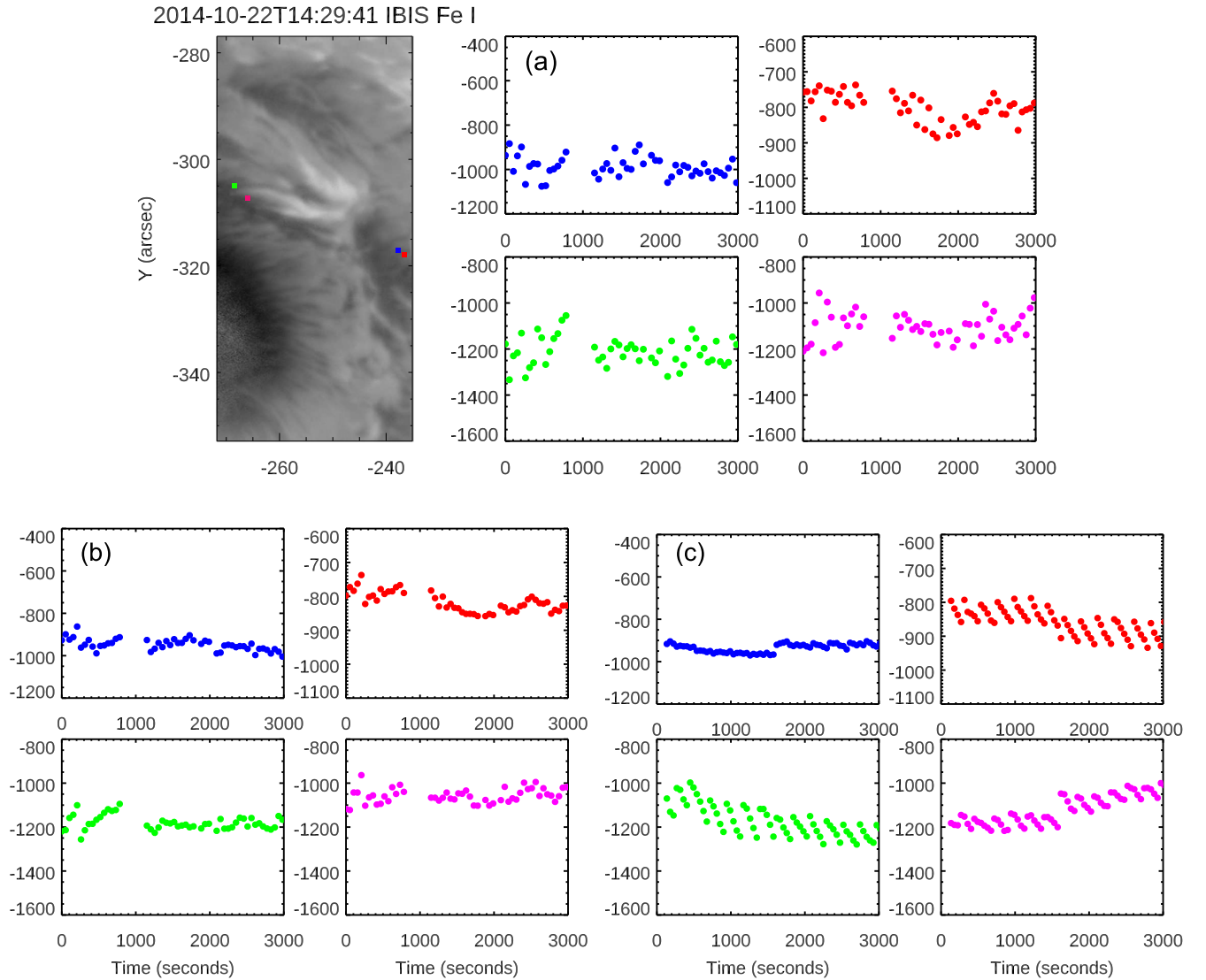
Figure 12. (a) Evolution of the photospheric longitudinal magnetic field during the X1.6 flare in the four locations analyzed in Figure 8. The map in the left panel refers to the Fe I line core. (b) Evolution of the photospheric longitudinal magnetic field during the X1.6 flare in four different 11×11 boxes obtained with P-MILOS using the IBIS data. (c) Temporal evolution of the longitudinal magnetic field recorded by SDO/HMI in four locations corresponding to the boxes used to obtain the plots shown in panels (a).

during this flare (Thalmann et al. 2015; Veronig & Polanec 2015). It is worth mentioning the small displacement of the flare ribbon observed in the region of the magnetic polarity intrusion.

4. Discussion of the Results

The possibility of having simultaneous measurements of the magnetic field in two different solar atmospheric layers allows us to investigate the distribution and eventually the variation of the magnetic field at different heights and therefore how the instabilities that are associated with the flaring process take place.

The investigation carried out in this work is framed in this scenario. Using a still rare data set of spectropolarimetric measurements relevant to data acquired during a confined X1.6 flare by the IBIS instrument along the profiles of the photospheric Fe I 617.30 nm line and of the chromospheric Ca II 854.2 nm line, we analyzed the configuration and

evolution of the magnetic field during a time interval of about one hour and ten minutes after the flare peak.

Figure 5 shows the Stokes profiles inferred from the spectropolarimetric data acquired along the Fe I 617.30 nm line and the chromospheric Ca II 854.2 nm line in three selected areas corresponding to different photospheric features, all included in the flare ribbon observed in the chromosphere. Taking into account that a similar analysis has been carried out on several other areas in the FOV (not shown in this paper), we can summarize the main results of this analysis as follows:

1. In the photosphere the profiles of Q and U show different shapes in the three selected areas;
2. The Stokes parameters Q and U are stronger in the chromosphere than in the photosphere;
3. They show profiles unrelated to each other.

The difference in the shape of the Q and U profiles might be related to the different photospheric features that have been chosen (inside a pore, in a penumbral filament, and in a bright
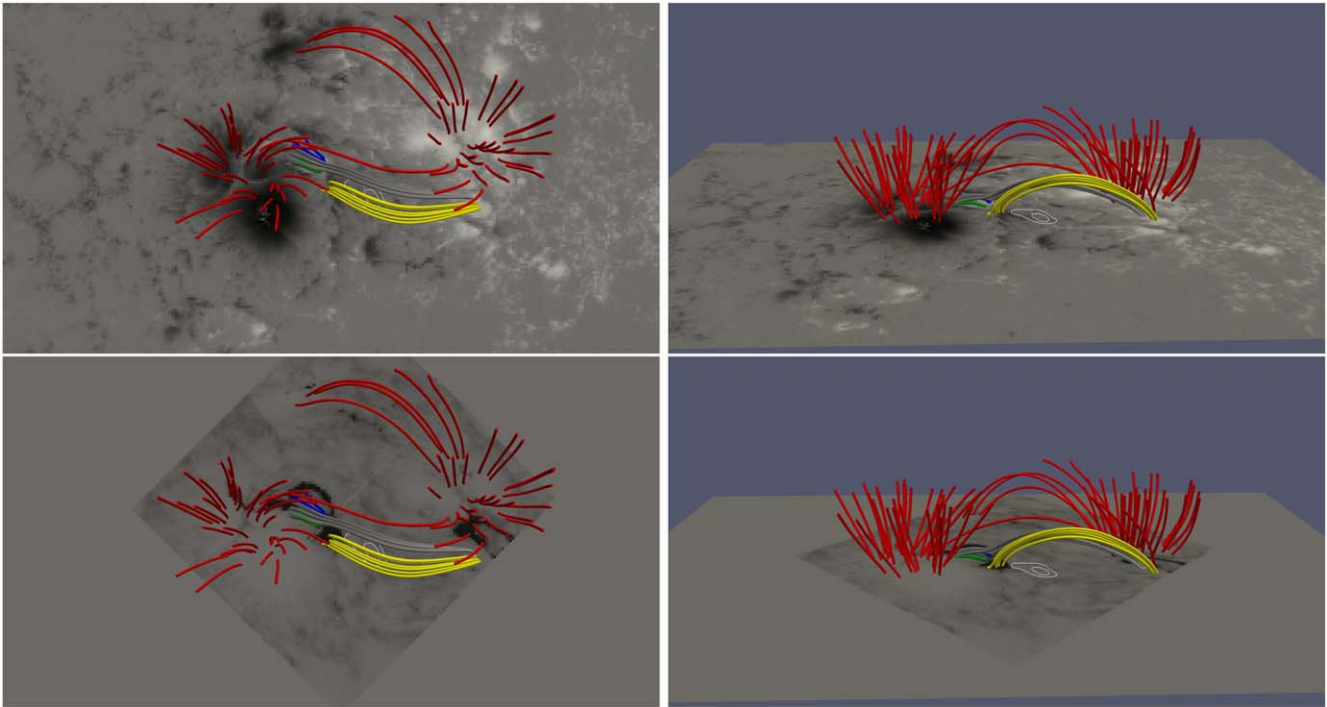
Figure 13. NLFF extrapolation obtained from the vector magnetograms taken by SDO/HMI at 14:00 UT. The left and right panels show the top and side views, respectively. In the top panels, the line-of-sight component of the magnetic field, used as a boundary condition for extrapolation, is shown as the bottom layer. In the bottom panels, the IRIS image taken at 14:06 UT on a reverse color scale has been displayed as the bottom layer of the extrapolated field lines. The contours of the RHESSI image at 80% and 90% of the maximum intensity at 14:29 UT are overplotted on the bottom layer. Lines with different colors indicate flux tubes with different connectivity.

photospheric area at the border of the penumbra): it can be expected that these diverse features are affected differently by the magnetic field restructuring at a time close to the flare peak. Higher Q and U Stokes parameters in the chromosphere are indicative of a predominance of the horizontal magnetic field component in this layer—a result in agreement with previous studies carried out by Harvey (2012). The poor correlation between the photospheric and chromospheric Stokes profiles might be a consequence of the different magnetic field inclination mentioned above, which is also confirmed by the results of the NLFF magnetic field extrapolation shown in Figure 13.

Regarding the analysis of the distribution and evolution of linear and circular polarization detected in the chromospheric Ca II 854.2 nm line (see Figure 6), our results indicate that their intensity shows a significant variation, characterized by a decreasing trend during the flare evolution, likely due to decreasing emission during the flare gradual phase—a hypothesis that is substantiated by the mean intensity trend reported in Figures 8(d) and 9.

The Ca II 854.2 nm line data have also been used to infer the chromospheric magnetic field distribution and changes using the WFA, providing the result that the region of positive intrusion (located northwest of the following sunspot), exhibits an LOS magnetic field strength of the order of 100–200 G, while the surrounding negative region shows values of ~ -100 G.

A further analysis was carried out in order to verify whether, during this X1.6 flare, it was also possible to detect any temporal variation of the chromospheric magnetic field, which could be described to first order by a B_{LOS} step function (see, e.g., Sudol & Harvey 2005; Kleint 2017). Our analysis, besides

confirming previous results reported in the literature of the occurrence of changes in B_{LOS} at certain locations during the event (see, e.g., Cliver et al. 2012; Burtseva et al. 2015; Kleint 2017; Castellanos Durán et al. 2018), allowed us to find that most of the variations occurred within 3 minutes after the peak of the flare, in a time interval initially encompassing the tail of the impulsive phase, as indicated by the RHESSI count rates in the nonthermal energy range of 25–50 keV (see Figure 2). In this respect, we stress that the chromospheric changes found through the WFA are confirmed by the results of the STiC inversion, as clearly shown in Figure 8 (bottom panels) and Figure 9 (cyan and light brown pixels).

However, we note that other mechanisms, such as changes in opacity due to temperature or density variations during the flare evolution, could also contribute to the observed variations in B_{LOS}. In fact, we know that the Ca II 854.2 nm line is a challenging line to understand and analyze because of its low magnetic sensitivity (e.g., Felipe et al. 2021). On one hand it allows us to use the weak-field approximation to infer the magnetic field from this line even in atmospheres with strong magnetic fields, such as sunspots, flares, etc. On the other hand, opacity effects can also influence the Ca II 854.2 nm line and cause apparent magnetic field fluctuations. For example, Bellot Rubio et al. (2000) showed with the simultaneous inversion of three Fe I lines, which are particularly sensitive to the magnetic field, that the magnetic field oscillations they found were caused by opacity fluctuations that shifted the height of line formation up and down in an atmosphere with a vertical gradient of magnetic field strength. Similarly, Felipe et al. (2014) found that the intensity variations of the Fe I 630.15 nm line were produced by opacity fluctuations rather than intrinsic
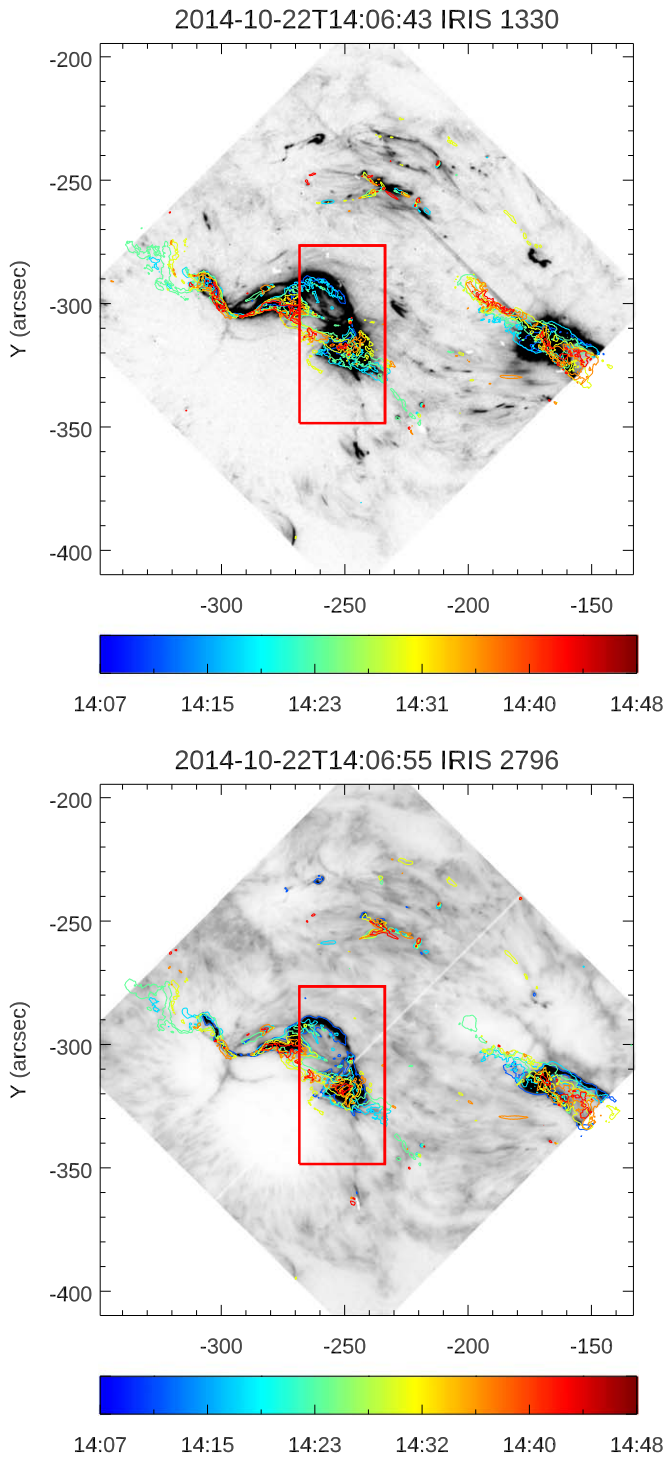
Figure 14. Top: IRIS 133 nm SJ negative image (relevant to C II lines). Bottom: IRIS 279.6 nm SJ negative image (relevant to Mg II lines). The contours show the evolution in time of the isophotes at DN = 1000 for C II 133 nm and at DN = 1500 for Mg II 279.6 nm. The corresponding time of each isophote is shown in the color bar. The IBIS FOV is indicated with a red box.

that they had small differences in the sensitivity at different optical depths, although the RFs had similar shapes. Moreover, the RFs are model-dependent, so it could be possible that in a complex flaring atmosphere the sensitivity of the line changes with the flare evolution. Comparing the RFs to perturbations in the LOS magnetic field and temperature, Kuridze et al. (2018) found a change in the sensitivity of the Ca II line between flaring and nonflaring atmospheres. During the flare, the Ca II 854.2 nm line was more sensitive to the lower atmosphere where the magnetic field was stronger. After the flare peak, the line shifted its sensitivity to the higher levels of the atmosphere where the magnetic field is weaker. Similarly, Yadav et al. (2021) found that the Ca II line increased its sensitivity in the deeper layers, where the magnetic field was relatively stronger, in some pixels near the footpoint of a magnetic loop during a C-class flare. Thus, we cannot rule out that a change in the sensitivity of the Ca II line could influence the evolution of the longitudinal magnetic field and its apparent variation after the flare peak.

In our study, we also analyzed the Fe I 617.30 nm data acquired by IBIS to investigate the photospheric B_{LOS} distribution and, using the Milne–Eddington Stokes inversion code P-MILOS, we obtained maps of the longitudinal magnetic field that show a detailed view of the magnetic configuration around the positive intrusion, as well as a very good agreement with the HMI magnetogram (compare Figure 4, first panel, with Figure 7, second panel).

The Fe I 617.30 nm data set was also used to investigate whether stepwise changes in B_{LOS} occurred at the photospheric level as well. The comparison between Figures 8 and 11 shows that in the photosphere there is not the same trend observed in the chromosphere for the analyzed pixels. This discrepancy has been also validated by comparing the results of the P-MILOS inversion of the IBIS Fe I 617.30 nm data with the HMI data (see Figures 12(a) and (b)), which conversely exhibit a rather consistent behavior.

In addition, taking into account the previous analysis of this flare carried out by Castellanos Durán et al. (2018; see their Figure 2, FL11), which showed that stepwise changes were detected in a more compact region (see, e.g., Figure 11), we were able to confirm that this discrepancy in spatial distribution is attributable to the different and longer time interval used by those authors, beginning well before the flare peak.

To better highlight the different spatial distributions of the changes in B_{LOS} in the photosphere and chromosphere, we show in Figure 15 a comparison between the photospheric and chromospheric maps with the areas of changes in B_{LOS} overplotted (second and third panels) and a map reporting only the areas where B_{LOS} changes (fourth panel). From inspection of the fourth panel of Figure 15, it is evident that the chromospheric changes are mainly concentrated on the flare ribbon, a result that agrees with previous analyses (see, e.g., Figure 4 in Kleint 2017), while the photospheric changes seem to be sparsely distributed in most of the analyzed FOV. In this respect, we would like to emphasize the results presented in Figures 11(c) and (d), based on the analysis of HMI data. These panels indicate that the spatial distribution of pixels exhibiting changes appears to be dependent on the time interval used for the analysis: sparse for a shorter time interval, beginning just after the flare peak, and compact for a longer time interval encompassing the flare peak. This also implies that we cannot rule out the possibility that the spatial distribution of the
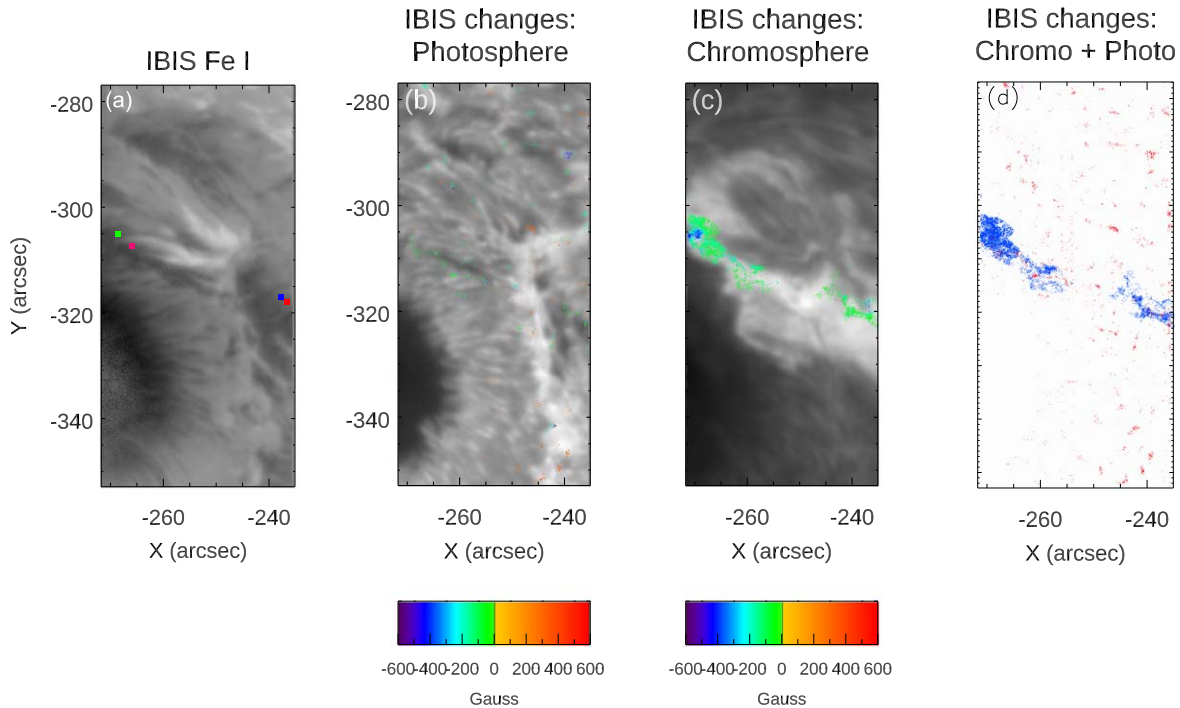
temperature oscillations. This issue could also affect the inference of the magnetic field from the WFA.

The diagnostic potential of the Ca II line is also a subject of study, because the response functions (RFs) can reveal how the height of line formation may vary. For example, Quintero Noda et al. (2016) computed the RFs for Ca II using different semiempirical models (FALC, HSRA, VALC, etc.) and found

Figure 15. (a) Map of the LOS magnetic field in the photosphere inferred from IBIS data. (b) Distribution of the changes in LOS magnetic field in the photosphere overplotted on a photospheric image. (c) Distribution of the changes in LOS magnetic field in the chromosphere overplotted on a chromospheric image. (d) Distribution of the changes in LOS magnetic field in the photosphere (red symbols) and in the chromosphere (blue symbols).

chromospheric changes we found may be partially biased by the limited IBIS observing interval.

Moreover, our analysis has shown that there is no clear evidence of changes in B_{LOS} along the PIL surrounding the positive magnetic intrusion because the changes appear to occur at least at $10''$ away from the PIL, a result different from the one reported by Kleint (2017), who indicated that photospheric changes were located along the PIL. However, on this issue we can recall that a careful analysis was successively carried out by Castellanos Durán et al. (2018) on 75 flares characterized by different classes, ranging between B6.2 and X6.9, where the relationship between changes in magnetic field and the PIL was investigated. They found that, as a general rule, there is an exponential decrease in the number of changes in magnetic field with increasing distance from the PIL. Interestingly, if we examine Figure 4 in Castellanos Durán et al. (2018), we can see that, while changes in B_{LOS} can be very compact and evident along the main PIL (see, e.g., FL8, FL26, FL46), a more sparse and less evident distribution of changes in B_{LOS} can be detected along the PIL of magnetic intrusions (see, for instance, FL7, FL11—corresponding to the flare analyzed in this work, FL23, FL48). This behavior might be indicative of different changes in the shear angle of magnetic field along the main PIL with respect to the PIL surrounding a magnetic intrusion.

Finally, the results of the NLFF extrapolation carried out using the vector magnetograms taken by SDO/HMI some minutes before the flare onset, compared with the time evolution of the isophotes inferred from IRIS data, and with the RHESSI image acquired at 14:29 UT, suggest that the FOV observed by IBIS might correspond to the area affected by the initial energy release.

5. Conclusions

In recent years, it has become clear that during solar flares the chromospheric magnetic field can show permanent changes (see, e.g., Kleint 2017), a result that was previously stressed for the photospheric magnetic field (see, e.g., Cameron & Sammis 1999; Kosovichev & Zharkova 1999, 2001; Sudol & Harvey 2005; Cliver et al. 2012; Burtseva et al. 2015, Castellanos Durán et al. 2018, Zuccarello et al. 2020; and references therein).

In this work, using one of the few available spectro-polarimetric data sets acquired in the Ca II 854.2 nm line by the IBIS instrument, we provide evidence that, during an X1.6 flare that occurred in AR NOAA 12192 on 2014 October 22, the changes in chromospheric field or opacity detected at certain locations along one of the flare ribbons show a similar behavior to those observed by Kleint (2017).

A first comparison between the photospheric Fe I 617.30 nm line and the chromospheric Ca II 854.2 nm line data indicates that selecting areas characterized by different photospheric features, but still within the chromospheric ribbon, the Q and U profiles show different trends, being unrelated to each other and stronger in the chromosphere.

Our investigation aimed at determining the chromospheric magnetic field distribution and changes using the weak-field approximation. This analysis provided an indication of a stronger LOS magnetic field intensity in the area of positive magnetic field intrusion than in the surrounding negative-polarity region that characterized the following sunspot of AR NOAA 12192.

Moreover, the WFA analysis has shown that, similarly to other events analyzed by other authors (see, e.g., Kleint 2017), the chromospheric B_{LOS} shows changes at certain locations. In our observations these changes occur during the first three minutes of our data set, framed within the tail of the flare impulsive phase. This result was validated by a further analysis consisting in the inversion by means of the STiC code of the same pixels previously treated with the WFA. The comparison

between the results obtained with the two methods appears to be very satisfactory (see Figure 8, bottom panels, and Figure 9). However, it is important to stress that the time window of our observation does not cover the preflare phase, and therefore it is not suitable to assess the presence of stepwise changes.

The study of the photospheric magnetic field evolution was carried out by means of the analysis of the Fe I 617.30 nm data set, showing that in the photosphere there is a different distribution and trend to that observed in the chromosphere (compare Figure 8 with Figure 11). Also for the photosphere we tried to validate our findings by comparing the results of the P-MILOS inversion of the IBIS Fe I 617.30 nm data with the HMI data, obtaining a good agreement. As a future step, we plan to invert both the photospheric Fe I 617.30 nm and chromospheric Ca II 854.2 nm data in a coupled inversion using STiC.

On the basis of the results obtained from our analysis, we can conclude that the changes at chromospheric levels, as far as their location is concerned, i.e., along the flare ribbons, seem to confirm previous results (e.g., Kleint 2017), although we cannot exclude other mechanism that can produce similar effects. On the other hand, in the photosphere, despite the IBIS FOV including a magnetic polarity intrusion, representing therefore a suitable test-bed to verify whether these changes occur along the PIL as reported in other observations, there is no direct evidence of this circumstance.

This discrepancy might perhaps be explained in terms of a difference in the PIL characteristics: for instance, in the analysis of Kleint (2017) changes occurred probably along the main PIL between the flare ribbons, while in our analysis the PIL surrounds the polarity intrusion. In this respect, we have suggested that this hypothesis seems to be supported by the analysis carried out by Castellanos Durán et al. (2018), which included also some samples of magnetic intrusions. In any case, we believe that thanks to our analysis this circumstance has been highlighted and it surely deserves to be further investigated in the future.

Using the NLFF field extrapolation we could verify the complexity of the AR and the different connectivities between the region observed by IBIS and the surrounding magnetic field. Indeed, by comparing the magnetic field line connectivity with the temporal evolution of the isophotes of the flare ribbons observed by IRIS, we could expect that the interaction between the positive intrusion observed within the IBIS FOV and the overlying magnetic field might have had a role during the flare, and therefore the fact that we do not observe photospheric B_{LOS} changes in this area is noteworthy. In this respect, taking into account that the isophotes' distribution with time (see Figure 14) indicates quite a slow evolution of the ribbons, we recall that Veronig & Polanec (2015) and Thalmann et al. (2015) found that the considered event shows a great initial separation of the ribbon, but no significant displacement during the flare.

In conclusion, if we consider the general scenario of the flare, it appears difficult to include our findings in the classical post-reconnection process of magnetic field line rearrangement. In this respect, our finding about the paucity of evidence or unclear evidence of photospheric changes in B_{LOS} around the PIL surrounding the positive magnetic intrusion inside the negative polarity could help in improving our understanding of the role played by the change in connectivity in these regions, and this surely deserves further investigations. Moreover, this

aspect could be linked to the peculiar magnetic configuration of the AR and the paucity of eruptive events occurring there (see Vasantharaju et al. 2023).

Careful data mining in the data archives of high-resolution instruments, such as the IBIS-A (Ermolli et al. 2022) relevant to past IBIS observations at the DST, may provide other data sets to be investigated to further elucidate the behavior of changes in magnetic field during flares. It is clear, however, that a more sound and complete interpretation of events of this kind will be possible when the new generation of ground-based telescopes of the class of 4 m, i.e., the National Science Foundation's Daniel K. Inouye Solar Telescope (DKIST; Rimmele et al. 2020) and the European Solar Telescope (EST; Jurčák et al. 2019; Quintero Noda et al. 2022) provide higher-resolution spectropolarimetric data.

ORCID iDs

F. Zuccarello ⓘ https://orcid.org/0000-0003-1853-2550
S. L. Guglielmino ⓘ https://orcid.org/0000-0002-1837-2262
S. Criscuoli ⓘ https://orcid.org/0000-0002-4525-9038
P. Romano ⓘ https://orcid.org/0000-0001-7066-6674

References

Bellot Rubio, L. R., Collados, M., Ruiz Cobo, B., et al. 2000, ApJ, 534, 989
Bellot Rubio, L., Cabrera Morales, M., & Cobos Carrascosa, J. P. 2022, Proc. SPIE, 12189, 121890I
Burtseva, O., Martínez-Oliveros, J. C., Petrie, G. J. D., et al. 2015, ApJ, 806, 173
Cameron, R., & Sammis, I. 1999, ApJL, 525, L61
Castellanos Durán, J. S., & Kleint, L. 2020, ApJ, 904, 96
Castellanos Durán, J. S., Kleint, L., & Calvo-Mozo, B. 2018, ApJ, 852, 25
Cavallini, F. 2006, SoPh, 236, 415
Ceppatelli, G., & Briand, C. 2001, MmSAI, 72, 558
Chen, H., Zhang, J., Ma, S., et al. 2015, ApJL, 808, L24
Cliver, E. W., Petrie, G. J. D., & Ling, A. G. 2012, ApJ, 756, 144
Collados, M., López, R., Páez, E., et al. 2012, AN, 333, 872
de la Cruz Rodríguez, J., Leenaarts, J., Danilovic, S., et al. 2019, A&A, 623, A74
de la Cruz Rodríguez, J., & van Noort, M. 2017, SSRv, 210, 109
De Pontieu, B., Title, A. M., Lemen, J. R., et al. 2014, SoPh, 289, 2733
del Toro Iniesta, J. C. 2007, Introduction to Spectropolarimetry (Cambridge: Cambridge Univ. Press)
Elmore, D. F., Lites, B. W., Tomczyk, S., et al. 1992, Proc. SPIE, 1746, 22E

Ermolli, I., Giorgi, F., Murabito, M., et al. 2022, A&A, 661, A74
Felipe, T., Socas Navarro, H., Sangeetha, C. R., et al. 2021, ApJ, 918, 47
Felipe, T., Socas-Navarro, H., & Khomenko, E. 2014, ApJ, 795, 9
Fontenla, J. M., Avrett, E. H., & Loeser, R. 1993, ApJ, 406, 319
Harvey, J. W. 2006, in ASP Conf. Ser. 358, Solar Polarization 4, ed.
     R. Casini & B. Lites (San Francisco, CA: ASP), 419
Harvey, J. W. 2012, SoPh, 280, 69
He, H., Wang, H., & Yan, Y. 2011, JGRA, 116, A01101
Hoeksema, J. T., Liu, Y., Hayashi, K., et al. 2014, SoPh, 289, 3483
Hurford, G. J., Schmahl, E. J., Schwartz, R. A., et al. 2002, SoPh, 210, 61
Jaeggli, S. A., Lin, H., Mickey, D. L., et al. 2010, MmSAI, 81, 763J
Judge, P. G., Kleint, L., & Sainz Dalda, A. 2015, ApJ, 814, 100
Jurčák, J., Collados, M., Leenaarts, J., et al. 2019, AdSpR, 63, 1389
Kleint, L. 2012, ApJ, 748, 138
Kleint, L. 2017, ApJ, 834, 26
Kleint, L., Wheatland, M. S., Mastrano, A., & McCauley, P. I. 2018, ApJ, 865, 146
Kosovichev, A. G., & Zharkova, V. V. 1999, SoPh, 190, 459
Kosovichev, A. G., & Zharkova, V. V. 2001, ApJL, 550, L105
Kuckein, C., Collados, M., Sainz, R. M., & Ramos, A. A. 2015, in IAU Symp.
     305, Polarimetry: From the Sun to Stars and Stellar Environments
     (Cambridge: Cambridge Univ. Press), 73
Kuridze, D., Henriques, V. M. J., Mathioudakis, M., et al. 2018, ApJ, 860, 10
Landi Degl'Innocenti, E. 2008, Fisica Solare, UNITEXT (Milan: Springer)
Lemen, J. R., Title, A. M., Akin, D. J., et al. 2012, SoPh, 275, 17
Libbrecht, T., de la Cruz Rodríguez, J., Danilovic, S., et al. 2019, A&A,
     621, A35
Lin, R. P., Dennis, B. R., Hurford, G. J., et al. 2002, SoPh, 210, 3
Ling, A. G., & Kahler, S. W. 2020, ApJ, 891, 54
Martínez González, M. J., & Bellot Rubio, L. R. 2009, ApJ, 700, 1391
Martínez Pillet, V., Collados, M., Sánchez Almeida, J., et al. 1999, in ASP
     Conf. Ser. 183, High Resolution Solar Physics: Theory, Observations, and
     Techniques, ed. T. R. Rimmele, K. S. Balasubramaniam, & R. R. Radick
     (San Francisco, CA: ASP), 264

Metcalf, T. R., Leka, K. D., & Mickey, D. L. 2005, ApJL, 623, L53
Penn, M. J., & Kuhn, J. R. 1995, ApJL, 441, L51
Pesnell, W. D., Thompson, B. J., & Chamberlin, P. C. 2012, SoPh, 275, 3
Quintero Noda, C., Schlichenmaier, R., Bellot Rubio, L. R., et al. 2022, A&A,
     666, A21
Quintero Noda, C., Shimizu, T., de la Cruz Rodríguez, J., et al. 2016, MNRAS,
     459, 3363
Reardon, K. P., & Cavallini, F. 2008, A&A, 481, 897
Rimmele, T. R. 2004, Proc. SPIE, 5490, 34
Rimmele, T. R., Warner, M., Keil, S. L., et al. 2020, SoPh, 295, 172
Romano, P., Elmhamdi, A., Falco, M., et al. 2018, ApJL, 852, L10
Romano, P., Elmhamdi, A., & Kordi, A. S. 2019, SoPh, 294, 4
Romano, P., Guglielmino, S. L., Costa, P., et al. 2022, SoPh, 297, 7
Romano, P., Zuccarello, F., Guglielmino, S. L., et al. 2015, A&A, 582, A55
Scharmer, G. B., Bjelksjo, K., Korhonen, T. K., Lindberg, B., & Petterson, B.
     2003, Proc. SPIE, 4853, 341
Scharmer, G. B., Narayan, G., Hillberg, T., et al. 2008, ApJL, 689, L69
Scherrer, P. H., Schou, J., Bush, R. I., et al. 2012, SoPh, 275, 207
Sudol, J. J., & Harvey, J. W. 2005, ApJ, 635, 647
Sui, L., Holman, G. D., & Dennis, B. R. 2004, ApJ, 612, 546
Thalmann, J. K., Su, Y., Temmer, M., & Veronig, A. M. 2015, ApJL, 801, L23
Toriumi, S., & Wang, H. 2019, LRSP, 16, 3
Vasantharaju, N., Zuccarello, F., Ferrente, F., et al. 2023, ApJ, 950, 183
Veronig, A. M., & Polanec, W. 2015, SoPh, 290, 2923
Vissers, G. J. M., Danilovic, S., de la Cruz Rodríguez, J., et al. 2021, A&A,
     645, A1
Wang, H., & Liu, C. 2015, RAA, 15, 145
Wöger, F., von der Lühe, O., & Reardon, K. 2008, A&A, 488, 375
Yadav, R., Díaz Baso, C. J., de la Cruz Rodríguez, J., Calvo, F., & Morosin, R.
     2021, A&A, 649, A106
Yan, Y., & Li, Z. 2006, ApJ, 638, 1162
Yang, S., Zhang, J., & Xiang, Y. 2014, ApJL, 793, L28
Zuccarello, F., Guglielmino, S. L., Capparelli, V., et al. 2020, ApJ, 889, 65